Check for updates

ADVANCED MATERIALS TECHNOLOGIES
www.advmattechnol.de

Printing, Characterizing, and Assessing Transparent 3D Printed Lenses for Optical Imaging

Liam M. Rooney, Jay Christopher, Ben Watson, Yash Susir Kumar, Laura Copeland, Lewis D. Walker, Shannan Foylan, William B. Amos, Ralf Bauer, and Gail McConnell*

High-quality lens production has involved subtractive manufacturing methods for centuries. These methods demand specialist equipment and expertise that often render custom high-grade glass optics inaccessible. A low-cost, accessible, and reproducible method is developed to manufacture high-quality three dimensional (3D) printed lenses using consumer-grade technology. Various planoconvex lenses are produced using a consumer-grade 3D printer and low-cost spin coating setup, and printed lenses are compared to commercial glass counterparts. A range of mechanical and optical methods are introduced to determine the surface quality and curvature of 3D printed lenses. Amongst others, high-resolution interference reflection microscopy methods are used to reconstruct the convex surface of printed lenses and quantify their radius of curvature. The optical throughput and performance of 3D printed lenses are assessed using optical transmissivity measurements and classical beam characterization methods. It is determined that 3D printed lenses have comparable curvature and performance to commercial glass lenses. Finally, the application of 3D printed lenses is demonstrated for brightfield transmission microscopy, resolving sub-cellular structures over a 2.3 mm field-of-view. The high reproducibility and comparable performance of 3D printed lenses present great opportunities for additive manufacturing of bespoke optics for low-cost rapid prototyping and improved accessibility to high-quality optics in low-resource settings.

1. Introduction

Additive manufacturing, in particular three dimensional (3D) printing, has resulted in a range of innovative open hardware solutions for optical imaging applications. The variety of printing modalities, commitment to open sharing by users, low barrier-to-entry, and rapid evolution of 3D printing technologies have provided new opportunities to make imaging more accessible, particularly in low-resource settings.[1–4] Open microscopy initiatives have aimed to provide improved access to 3D printed microscopy hardware for use in the field or in rapid clinical diagnostics, such as the OpenFlexure project.[5–8] However, such initiatives routinely focus on 3D printing the mechanical parts of the microscope, such as the chassis, focusing assemblies, or specimen mounts, mainly using fused deposition modeling (FDM) printing to manufacture parts from heated plastic filaments. The optical elements in these applications still use glass objects or plastic camera lenses. There is a need for accessible and robust methods to produce high-quality optical elements.

Optical imaging has relied on the use of ground glass lenses to manipulate light for centuries.[9–12] Manufacturing such glass lenses is a subtractive process that can be prohibitively expensive for custom optics, requires specialist equipment and expertise, and produces a product that is delicate and easily damaged. Additive manufacturing, specifically 3D printing, has the potential to mitigate each of these barriers. Recently, additive manufacturing methods using injection molding, magnetorheological, and molten glass printing have successfully

L. M. Rooney, L. Copeland, L. D. Walker, S. Foylan, W. B. Amos, G. McConnell
Strathclyde Institute for Pharmacy and Biomedical Sciences
University of Strathclyde
Glasgow G4 0RE, UK
E-mail: liam.rooney@strath.ac.uk

The ORCID identification number(s) for the author(s) of this article can be found under https://doi.org/10.1002/admt.202400043

© 2024 The Authors. Advanced Materials Technologies published by Wiley-VCH GmbH. This is an open access article under the terms of the Creative Commons Attribution License, which permits use, distribution and reproduction in any medium, provided the original work is properly cited.

DOI: 10.1002/admt.202400043

J. Christopher, R. Bauer
Department of Electronic and Electrical Engineering
University of Strathclyde
Glasgow G1 1XW, UK

B. Watson, Y. S. Kumar
Department of Physics
University of Strathclyde
Glasgow G4 0NG, UK

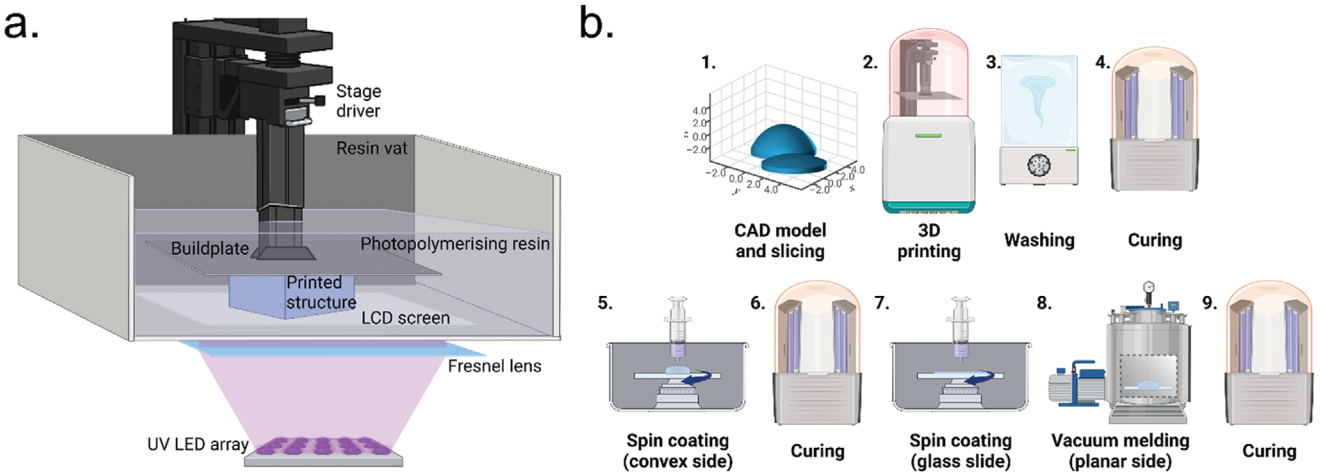

Figure 1. Methods for Manufacturing 3D Printed Lenses. a) A schematic of an mSLA printer. A collimated UV light source is projected onto an LCD screen which illuminates and masks individual print layers as the buildplate is lifted from a vat of photopolymerizing resin. b) A schematic of manufacturing process for 3D printed lenses. The initial design and printing process is conducted 1–4) before a series of spin coating and curing steps to provide a smooth lens surface and increased optical quality 5–9).

produced bespoke optical elements.[13–16] In the latter, glass filaments are heated and extruded as in FDM printing, annealed, and cured in a kiln to produce the final product. However, this process is prohibitively costly owing to the specialist equipment and expertise required to manipulate glass in such ways. Resin-based printing techniques provide a viable solution to create bespoke optical elements for use in open hardware and imaging applications.

A variety of resin-based printing methods are available, mainly based on stereolithography (SLA) techniques. Two-photon polymerization is routine for microfabrication of lenses, particularly for microlens arrays and x-ray imaging optics.[17–19] However, the requirement for specialist ultrashort pulsed laser sources and expensive printing instrumentation serves as a barrier to entry for these methods. Masked SLA (mSLA) printing is one of the most accessible SLA techniques.[20] This method uses a proprietary mix of methacrylate-based resin that is available in transparent and opaque forms and photoinitiated cross-linkers to polymerase under irradiation using 405 nm light. The illumination pattern is provided by an array of UV light emitting diodes, which can be collimated to provide homogeneous illumination over the entire build area. A liquid-crystal display (LCD) screen then masks the structure of discrete layers of the print design, changing in unison with the axial position of a build plate mounted to a motorized stage to create a printed 3D structure.[21,22] Recent studies have produced mSLA 3D printed lenses for spectrophotometry applications[23] and described methods to quantify their material properties;[24] however, the optical performance of 3D printed lenses remains uncharacterised. Current advances in consumer-grade mSLA printer technology enable printing with a lateral resolution of up to 18 µm and an axial resolution of up to 10 µm.

We aimed to create a robust method to manufacture and characterize the optical performance of transparent 3D printed high-quality bulk optics using a consumer-grade printer and commercially available resin. We used a low-cost mSLA 3D printer and employed a spin-coating method to render the lenses transparent by minimizing surface imperfections and reducing scattering and refraction from step structures originating from the printing process (the so-called "staircase effect"). We printed a range of planoconvex lenses of various optical prescriptions, characterised their surface profile in comparison to their commercial glass counterparts, and assessed their optical performance.

2. Experimental Section

2.1. 3D Printing

All 3D printing was conducted using a consumer-grade Mars 3 printer (Elegoo, China) fitted with a magnetic build plate attachment for easy print removal (Sovol, China). Clear resin (Clear Resin V4; Formlabs, USA) was used as the substrate for all prints. The print settings were optimized using the Cones of Calibration test print (TableFlip Foundry) and the print quality was verified using the Ameralabs Town test print (MB Labsamera, Lithuania) (Figure S1, Supporting Information). All lens prints were conducted using the parameters detailed in the Supporting Information, with the planar side of the lenses printed directly on the buildplate surface. **Figure 1** provides a graphical overview of the manufacturing process for 3D printed lenses.

Planoconvex lens designs (each with a lens diameter of 12.5 mm) were acquired from the manufacturer (Thorlabs, USA or Edmund Optics, USA) as STEP files. Files were imported into Fusion 360 (v2.0.16985; Autodesk, USA) and the polygon count was increased to the maximum available before being exported as STL files. Files were then imported into LycheeSlicer (v5.2.201; Mango3D, France), where the print parameters were applied, and the print files were exported as CTB files. The CTB lens files were printed with a raft surrounding the lens perimeter which provided a handling surface to avoid touching the lens surface. This increased the total diameter of the print to 25 mm, and ensured the print would fit in a standard 25 mm diameter optical mount (LMR1S; Thorlabs, USA). Four planoconvex lens prescriptions of different focal lengths (f) were selected, based on commercial glass counterparts; $f = +12.5$ mm (37-385; Edmund Optics, USA),

© 2024 The Authors. Advanced Materials Technologies published by Wiley-VCH GmbH

2365709x, 0, Downloaded from https://onlinelibrary.wiley.com/doi/10.1002/admt.202400043 by Welsh Assembly Government, Wiley Online Library on [08/05/2024]. See the Terms and Conditions (https://onlinelibrary.wiley.com/terms-and-conditions) on Wiley Online Library for rules of use; OA articles are governed by the applicable Creative Commons License

$f = +19.9$ mm (LA1074; ThorLabs, USA), $f = +35.0$ mm (37-791; Edmund Optics, USA), and $f = +49.8$ mm (LA1213; ThorLabs, USA).

Following printing, the lenses were removed from the magnetic build plate and washed with neat isopropanol (10592921; FisherScientific, USA) for 9 min in a Mercury X washing station (Elegoo, China). The prints were removed and carefully air-dried using a compressed Ultra Pure Duster (Thorlabs, USA) before a post-print UV curing step for 20 min in a Mercury X curing station (Elegoo, China).

2.2. Spin Coating and Lens Preparation

The printed lenses were rendered optically transparent by spin coating a thin layer of resin over both the curved and planar surfaces, minimizing layer artifacts and surface structures from the printing process. For the convex surface, a spin coater (L2001A3-E463; Ossila, UK) was fitted with a custom 3D printed chuck with a 25 mm diameter well to accommodate a printed lens. The printed lens was cleaned again prior to coating with 100% isopropanol, airdried using compressed air, and placed in the chuck. 100 µl of Clear UV Resin (4th Generation; VidaRosa, China) was deposited on the apex of the lenses (50 µl for $f = +49.8$ mm to accommodate the shallower curvature) and spun for 10 s at 2000 rpm. The coated lenses were stored in darkened conditions for 30 min to allow the liquid resin to settle and were subsequently cured for 20 min using the Mercury X curer as described above.

For the planar surface, the spin coater was fitted with a 76 mm × 26 mm microscope slide chuck and a clean microscope slide was placed in the chuck. A thin resin layer was created by depositing 100 µl of Clear Resin (v4; Formlabs, USA) on the slide and spinning for 10 s at 2000 rpm. The cleaned planar slide of the printed lens was carefully placed onto the resin-coated slide to avoid introducing air bubbles and was placed in a vacuum chamber (2 L, Bacoeng, USA) fitted with a vacuum pump (Capex 8C; Charles Austen Pumps Ltd, UK). The assembly was maintained under a vacuum on 0.9 bars for 30 min before curing for 20 min as described above. The melded lens-slide combination was stored at −20 °C for 3 min and carefully levered from the slide, relying on the differential thermal expansion of the glass and resin to remove the lens from the microscope slide.

2.3. Spin-Coat Thickness Measurements

To determine the thickness of the spin-coated layers, coumarin-30, a non-polar green-emitting organic fluorophore, was prepared as a 10 mM stock in 100% isopropanol and mixed with 1 mL of Clear UV Resin (4th Generation; VidaRosa, China) at a final concentration of 100 µM. Lenses from each of the four test prescriptions were spin-coated and cured as described above.

The thickness of the fluorescent spin-coated layer was measured by acquiring a 3D image stack using a confocal laser scanning microscope. An Olympus IX81 inverted microscope coupled to an FV1000 confocal laser scanning unit (Olympus, Japan) was used for imaging. Excitation of fluorescence was performed using a 488 nm argon laser (GLG3135; Showa Optronics, Japan) and fluorescence emission from coumarin-30 was detected by a photomultiplier tube (PMT) with a detection spectral window of 500–550 nm. Coated lenses were placed with the curved surface in contact with a Type 1.5 cover glass and imaged using a 10 × /0.4 numerical aperture (NA) objective lens (Olympus, Japan). All images were acquired at the axial Nyquist sampling rate for the imaging objective ($\Delta z = 1.53$ µm). The thickness of the fluorescent layer was measured using a linear plot profile of the fluorescence intensity in orthogonal (x,z and y,z) views of the 3D image stack using FIJI (v1.53t).[25] Analysis was conducted using three replicate printed lenses with each focal length.

2.4. White Light Interferometry and Stylus Profilometry

Methods for measuring the surface profile of planoconvex lenses include non-contact white light interferometry and contact stylus profilometry, with contact measurement approaches often only reporting the curvature of a linear trace instead of providing a 3D reconstruction of the specimen topology. Non-contact surface profiles were obtained using a white light interferometer (Wyko NT1100; Veeco Instruments Inc, USA) which used coherent light to generate interference fringes which were axially shifted through the optical surface, providing 2D surface roughness and uniformity measurements. The interferometer was used in a vertical scanning interferometry configuration where an internal translator axially scanned in one direction during the measurement as the in-built camera detector recorded each frame. The non-contact approach provides a ≈300 × 200 µm surface area measurement using a 20x objective, with a color gradient to indicate height (Δz) changes as well as read-out line profiles to provide sub-nanometre-scale surface roughness across the x and y axes of the specimen. The contact approach utilized a stylus profiler (Alpha-Step IQ; KLA Corp., USA) with a 5 µm tip diameter for 1D surface topology. The stylus profilometry technique provides millimeter-range 1D measurements with sub-nanometre height resolution for curvature and roughness analysis.

2.5. Interference Reflection Microscopy (IRM)

The underpinning theory of IRM relating to the imaging of plano-convex lenses has been explained elsewhere.[26,27] Briefly, the printed lens specimens were placed convex side down on a Type 1.5 cover glass, bridging the stage insert of an IX81 inverted microscope coupled to an FV1000 confocal laser scanning unit (Olympus, Japan). An 80/20 beamsplitter was used in place of the dichroic filter in the confocal microscope, which facilitated a configuration to detect reflected light from the specimen plane. A 458 nm argon laser (GLG3135; Showa Optronics, Japan) provided incident light, which was reflected from refractive index boundaries at the specimen plane (i.e., cover glass-air and air-lens interfaces). Reflected light from each interface coincided, leading to constructive and destructive interference depending on the optical path difference of the two reflected beams (**Figure 2a**). The resulting image provided a 2D projection of the 3D topography of the specimen surface, where interference orders were separated along the optical axis. Equations 1 and 2 describe the axial separation of destructive and constructive interference orders,

© 2024 The Authors. Advanced Materials Technologies published by Wiley-VCH GmbH

2365709x, 0, Downloaded from https://onlinelibrary.wiley.com/doi/10.1002/admt.202400043 by Welsh Assembly Government, Wiley Online Library on [08/05/2024]. See the Terms and Conditions (https://onlinelibrary.wiley.com/terms-and-conditions) on Wiley Online Library for rules of use; OA articles are governed by the applicable Creative Commons License

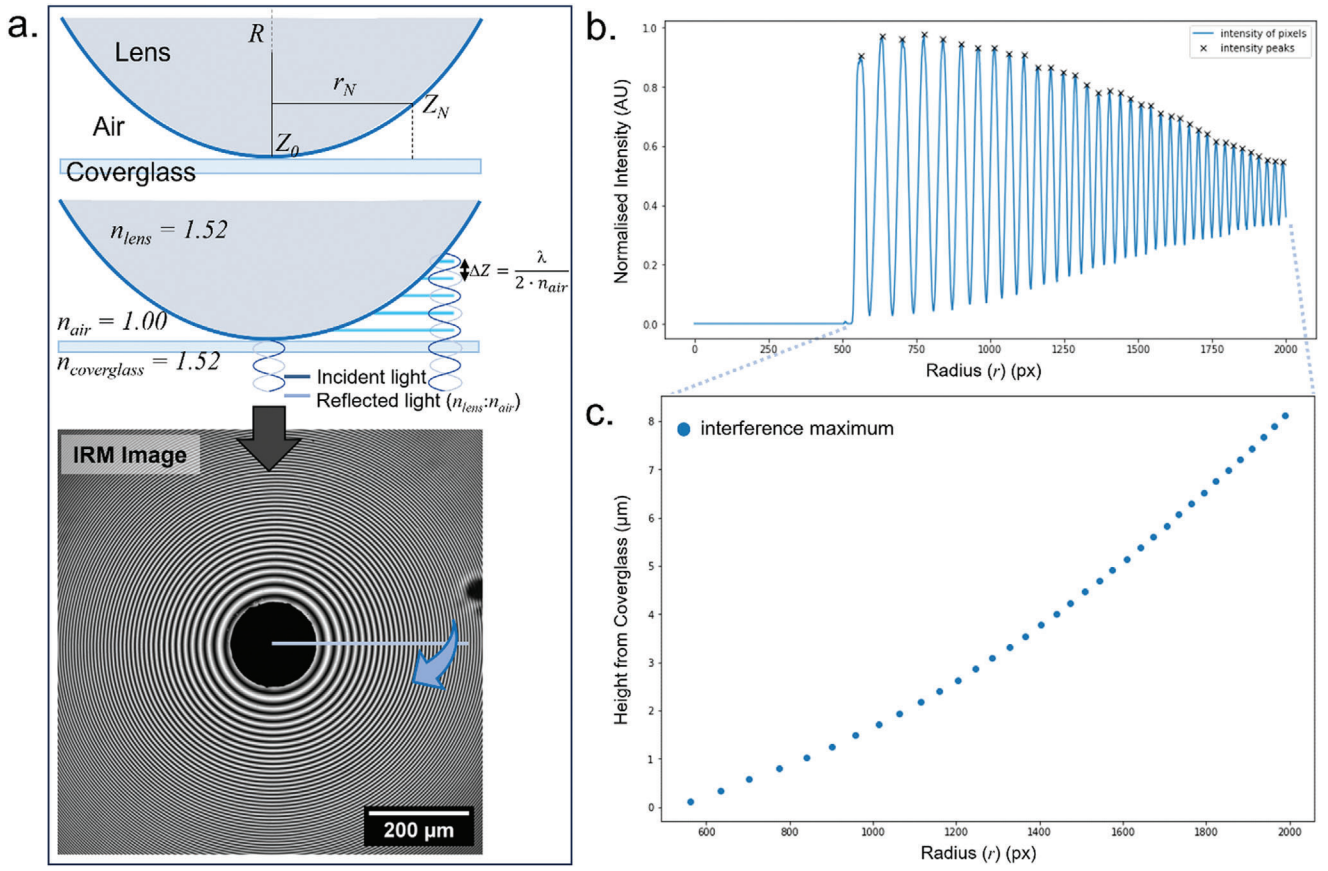

Figure 2. Reconstruction of Lens Curvature using Interference Reflection Microscopy (IRM). a) A schematic of the principles of IRM (not to scale). Refractive index boundaries reflect incident light and constructive/destructive interference occurs depending on the relative distance between reflective boundaries b) An IRM image of a lens was acquired, and a line intensity profile was measured. c) The axial position of the interference maxima (Equation 1) was plotted against the radial peak position from the line profile.

respectively,[28,29] where z = fringe spacing, N = order, λ = wavelength of incident light, and n_m = refractive index of the imaging medium.

$$z = N\left(\lambda/2n_m\right) \quad (1)$$

$$z = (N + 1/2)\left(\lambda/2n_m\right) \quad (2)$$

IRM images were acquired using a 10x/0.4 NA objective lens (Olympus, Japan) and the reflection signal was detected using a PMT with the detection limited to 458 ± 5 nm.

2.6. Reconstructing 3D Surface Curvature and Quantifying Radius of Curvature from 2D IRM Image Data

All computational analyses of IRM data were performed using FIJI and Python 3.8.10 (64-bit) in a Spyder IDE 5.3.2 environment on an Elitebook 840 G7 (Hewlett–Packard, USA) running a 64-bit Windows 10 Enterprise operating system with an Intel Core i5-10310U 1.70 GHz quad-core processor with 16 GB of 2666 MT/s DDR4 RAM.

The IRM image data were exported as OIB files and preprocessed using FIIJ. The images were cropped to ensure the apex of the lens was centered in the image, and a median filter (σ = 2) was applied to remove any high-frequency noise in the data. Images were contrast adjusted using the Contrast Limited Adaptive Histogram Equalization (CLAHE) plugin[30] (blocksize = 127, histogram bins = 256, maximum slope = 3.00) and converted to PNG files for analysis.

A custom Python pipeline[31] was created to generate 3D reconstructions of the surface of the lens specimens from 2D IRM images and calculate the median radius of curvature for each lens. Briefly, the Calibration script was first used to verify the correct feature detection parameters for IRM data. The position of the zeroth order minimum was taken as the center of the lens and the radius was noted as half the width of the image. The position of the intensity maxima along the radius was calculated using the find peaks function, iteratively optimizing the detection thresholds for peak height, distance, and prominence to ensure that each intensity maximum was detected. A line intensity profile noting the position of each interference maxima was generated along radius (r) (Figure 2b). The axial position of each interference maximum was calculated using Equation 1 and was plotted against distance to show the curvature of the lens (Figure 2c).

The surface curvature of each lens was reconstructed using the 3D Reconstruction script with the optimized setting for each lens applied from the Calibration script. The 3D convex surface was

© 2024 The Authors. Advanced Materials Technologies published by Wiley-VCH GmbH

2365709x, 0, Downloaded from https://onlinelibrary.wiley.com/doi/10.1002/admt.202400043 by Welsh Assembly Government, Wiley Online Library on [08/05/2024]. See the Terms and Conditions (https://onlinelibrary.wiley.com/terms-and-conditions) on Wiley Online Library for rules of use; OA articles are governed by the applicable Creative Commons License

reconstructed by assigning an axial position, as above, to each interference order detected along each radius (360 radii measured per image). The radius of curvature (R) value for each radius was calculated using Equation 3.[32]

$$R = r^2 + {z_N}^2/2 \cdot z_N \quad (3)$$

The measured radius of curvature for each lens was calculated using the Radius Analysis script in Python. The R-value for each radius was compiled into a histogram that compared the experimental measurements to the theoretical R (i.e., the manufacturer-quoted value for the lens design file used for printing). The maximum peak position from each histogram determined the R-value for each lens.

The measured and theoretical curvature data were plotted using Prism (v8.0.2) (GraphPad Software, USA).

2.7. Tolansky Interferometry

Tolansky interferometry, a mode of multiple-beam interference imaging, was used as an alternative means to visualize the curved topology at the apex of the convex surface of the 3D printed lenses. The principle of Tolansky interferometry relies on two opposing highly reflective surfaces (in this case, an aluminum-coated cover glass and an aluminum-coated 3D printed lens) which generate multiple reflected beams that undergo constructive and destructive interference.[33–35] The multiple beam combination acts to modify the Haidinger rings formed at the focus of the objective lens such that the nodal spacing is not altered, but the intensity distribution of the interference orders is changed. This effectively increases the axial resolution compared with IRM, such that topological features as small as 5 Å, or better, can be resolved within the interference maxima.[28] Moreover, uncoupling the reflective specimen from the reflective cover glass provides a means to translate the interference orders through the optical axis, in turn "scanning" the topography of the convex lens surface in a way that IRM cannot.

A 3D printed lens ($f = +19.9$ mm) and a Type 1.5 cover glass were vapor coated with a thin layer of aluminum using a thermal evaporator coating system (E306A; Edwards Vacuum, UK). Briefly, a small quantity of aluminum foil was heated on a tungsten filament under vacuum (1.0×10^{-5} Pa), depositing vaporized aluminum on the surface of the lens and cover glass.

A custom steel objective lens collar was fabricated and fitted to a 10 × /0.4 NA objective lens (Olympus, Japan). The aluminum-coated cover glass was bonded to the top of the collar using a thin layer of epoxy resin around the circumference of the objective lens housing. An adjustment screw was included in the collar to facilitate the positioning of the collar-cover glass assembly relative to the focal length of the objective lens (≈3.1 mm). The aluminum-coated lens specimen was suspended over the stage insert of an inverted IX81 microscope coupled to a confocal laser scanning unit (Olympus, Japan). Two glass microscope slide spacers were inserted to raise the test lens so that the modified objective underneath could be focused near to the lens surface. Tolansky interferometry was performed using the same reflection setup as in IRM experiments but employed z-scanning which uncoupled the specimen from the coverslip. Altering the relative distance between the cover glass and lens specimen resulted in axial translation of interference orders and provided a means of visualizing the curved apical surface by merging images acquired at different axial positions into a single hyperstack color-coded by depth using FIJI.

2.8. Optical Transmission Measurements

The percentage transmission of the printing resin was measured by comparing the mean intensity of transmitted light through resin blocks of varying thickness compared to the transmission through a single Type 1.5 cover glass. Resin blocks of thickness from 1 to 6 mm were printed using the optimized printing parameters used for lens printing. The blocks were placed on a Type 1.5 cover glass and imaged using an IX81 inverted microscope coupled to an FV1000 confocal laser scanning unit (Olympus, Japan) configured to detect scanned transmitted light. The transmissivity of unprocessed and processed blocks (i.e., naïve and spin-coated, respectively) was measured using three discrete wavelengths across the visible spectrum sequentially; a 458 nm argon laser, a 515 nm argon laser, and a 633 nm helium–neon laser (GLG3135; Showa Optronics, Japan). Images were acquired using a 4 × /0.1 NA objective lens (Olympus, Japan), with dimensions 64 × 64 pixels and Kalman averaging (n = 5 frames) to minimize contributions to the image from print structures. The mean intensity across the field was measured using FIJI and compared to the optical throughput of the cover glass alone. Linear fits were conducted using Prism.

2.9. Beam Profilometry

An optical setup was constructed to measure the focusing ability of 3D printed lenses compared to their commercial glass counterpart. A complete parts list is included in the Supporting Information. A 633 nm helium–neon laser source with an initial beam diameter measuring 600 µm was passed through a neutral density filter and was steered using two gimbal-mounted mirrors. The beam was expanded to a final diameter of 12.5 mm using two sequential beam expanders, first through a 2.5 × beam expander and then through a 7.5 × beam expander. The 3D printed lens was mounted in a fixed amount (LMR1S/M; Thorlabs, USA) and a dual scanning slit beam profiler was mounted on a linear translational stage to facilitate movement along the optical axis to map the beam diameter with respect to post-lens propagation distance. Perpendicular measurements (x and y axes) of the focused beam diameter ($1/e^2$) were measured at increments along the optical axis and compiled to provide a beam profile for three replicates of various planoconvex lens prescriptions. The $1/e^2$ beam waist radius (w_0) was calculated from the measured beam diameter and the Rayleigh Range (z_R) for each lens was calculated using Equation 4.[36] The Gaussian fit for a theoretical beam profile for each lens was calculated using Equation 5, where the beam diameter along the optical axis (w_z) is dictated by w_0, the wavelength of light (λ), and the distance from the measurement position (z) to the beam waist (z_0).

$$z_R = \pi \cdot {w_0}^2 \cdot n/\lambda \quad (4)$$

© 2024 The Authors. Advanced Materials Technologies published by Wiley-VCH GmbH

2365709x, 0, Downloaded from https://onlinelibrary.wiley.com/doi/10.1002/admt.202400043 by Welsh Assembly Government, Wiley Online Library on [08/05/2024]. See the Terms and Conditions (https://onlinelibrary.wiley.com/terms-and-conditions) on Wiley Online Library for rules of use; OA articles are governed by the applicable Creative Commons License

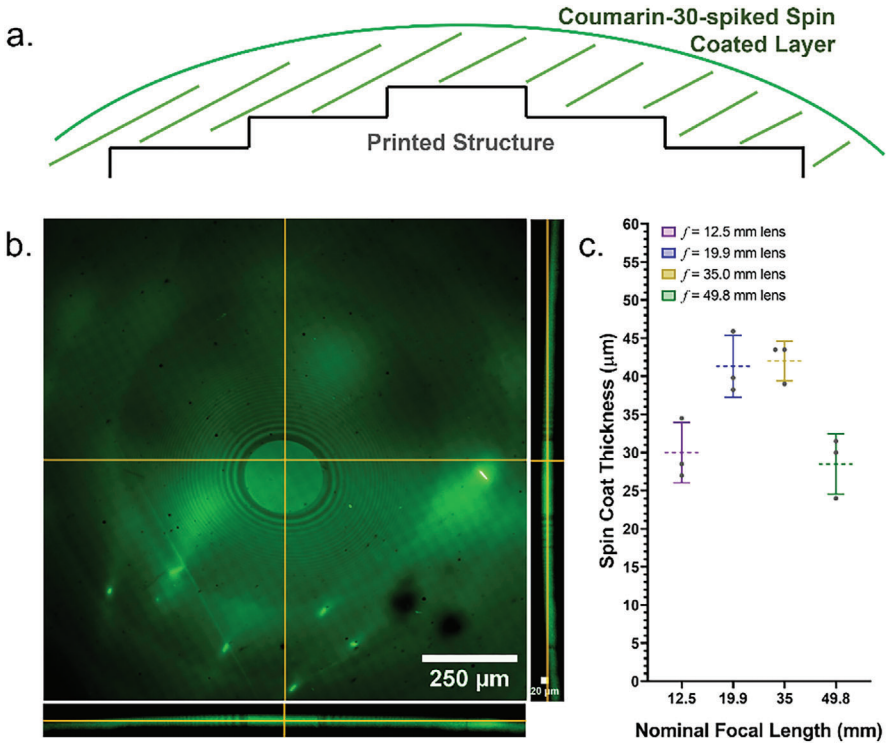

Figure 3. Thickness Measurements of the Spin-Coated Surface Layer of 3D Printed Lenses. a) A schematic of the spin-coated layer spiked with the organic dye, Coumarin-30 (not to scale) b) An average intensity projection and orthogonal views of the spin-coated layer of a 3D printed lens. c) Comparison of the spin coated layer thickness across three replicate 3D printed lenses for four lens prescriptions ($f = +12.5$ mm, purple; $f = +19.9$ mm, blue; $f = +35.0$ mm, yellow; $f = +49.8$ mm, green). The lenses had a median coat thickness ranging from 28.5 to 42.0 µm.

$$w_z = w_0\sqrt{1+\left(\lambda\left(z-z_0\right)/\pi {w_0}^2\right)^2} \quad (5)$$

Beam profiles were reconstructed using two scripts[37] based on the *NumPy, os, matplotlib.pyplot,* and *mpl_toolkits.axes_grid1* functions in Python 3.9.7 (32-bit) in a Spyder IDE 5.4.3 environment, then compiled and commented in a JupyterLab IDE 3.5.3 environment. All beam profile processing was conducted using Microsoft Windows 10 Pro running a 64-bit Windows 10 operating system with an Intel Core i7-7660U 2.50 GHz dual-core processor with 8 GB of 1867 MT/s DDR3 RAM.

2.10. Brightfield Transmission Microscopy

A brightfield transmission microscopy setup was constructed to demonstrate the performance of a 3D printed lens in an imaging setup. A complete parts list is included in the Supporting Information. A 10 mm stage micrometer with 50 µm intervals (R1L3S1P; ThorLabs, USA) and a thin section of linden tree stem (*Tilia europaea*) were imaged to assess the field of view and to determine the resolution of the system. A blue light-emitting diode (LED) source (λ = 470 nm) (M470L2-C1; ThorLabs, USA) was used to illuminate the specimen. Light from the LED was brought to the specimen using a 3D printed $f = +49.8$ mm planoconvex condenser lens (modeled on LA1213; ThorLabs, USA) and transmitted light was detected using a monochrome complementary metal-oxide-semiconductor (CMOS) camera (DCC3260M; ThorLabs, USA). Image acquisition was controlled via ThorCam (64-bit, v3.7.0) (ThorLabs, USA).

3. Results

3.1. Surface Characterisation of 3D Printed Lenses

3.1.1. Measuring the Thickness of Spin Coated Resin Layers on 3D Printed Lenses

The thickness of the spin-coated resin layer on the printed convex lens surface was measured using 3D confocal laser scanning microscopy. The coumarin-30-spiked VidaRosa Clear resin was spin-coated onto the convex surface using the same spin settings as for other lenses, creating a fluorescent resin layer (**Figure 3a**). A 3D confocal z-stack visualized the spin-coated layer relative to the lens surface (not fluorescent, ergo dark) (Figure 3b). The mean spin-coated thickness of the fluorescent resin was measured for three replicates of various lens prescriptions, with the spin-coat thickness routinely ranging from 25 to 45 µm (mean thicknesses; $f_{12.5\,\mathrm{mm}}$ = 30.00 µm, $f_{19.9\,\mathrm{mm}}$ = 41.31 µm, $f_{35.0\,\mathrm{mm}}$ = 42.00 µm, and $f_{49.8\,\mathrm{mm}}$ = 28.50 µm) (Figure 3c).

3.1.2. Comparing the Surface Curvature and Uniformity between 3D Printed and Commercial Glass Lenses

The surface curvature of 3D printed lenses was first measured by conventional means using a commercial white light

© 2024 The Authors. Advanced Materials Technologies published by Wiley-VCH GmbH

2365709x, 0, Downloaded from https://onlinelibrary.wiley.com/doi/10.1002/admt.202400043 by Welsh Assembly Government, Wiley Online Library on [08/05/2024]. See the Terms and Conditions (https://onlinelibrary.wiley.com/terms-and-conditions) on Wiley Online Library for rules of use; OA articles are governed by the applicable Creative Commons License

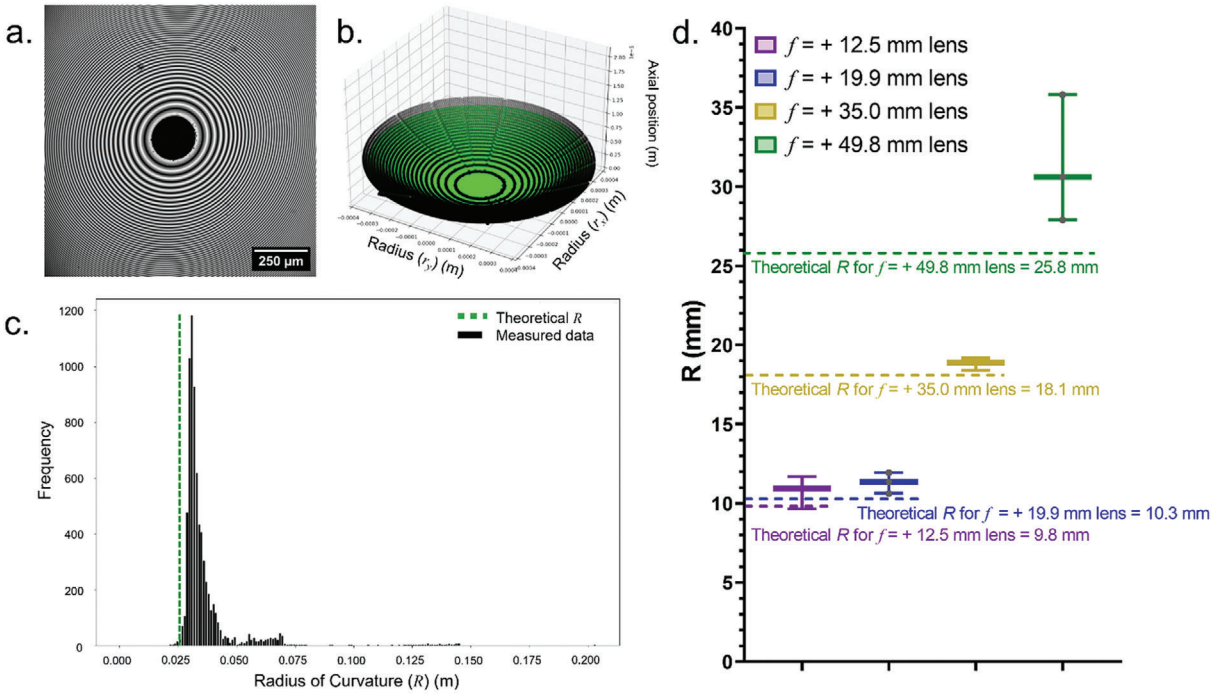

Figure 4. Radius of Curvature Measurements of 3D Printed Lenses using IRM. a,b) Surface reconstruction of a 3D printed lens from 2D IRM data using method presented in Figure 2. a) An IRM image of a 3D printed lens surface (λ = 458 nm). b) A 3D reconstruction of the printed lens surface (black datapoints) compared to the theoretical curvature from the print design (green). c) A histogram of the distribution of radius of curvature (R) values measured around the circumference of the lens (black) compared to the theoretical R (green) (See Equation 2). d) Measured radius of curvature values of three replicate 3D printed lenses for lens prescriptions (f = + 12.5 mm, purple; f = + 19.9 mm, blue; f = + 35.0 mm, yellow; f = + 49.8 mm, green).

interferometer and a stylus profilometer. However, white light interferometry usually requires higher reflective surfaces for accurate surface measurements, and stylus profilometry is typically restricted by measuring only orthogonal straight lines along the x and y axes of the lens (Figure S2, Supporting Information). An alternative method was required that accurately reconstructed the transparent 3D surface of the printed lenses, which provided a robust method to identify surface curvature defects that could impact optical performance.

Using the methods outlined in Figure 2, IRM image data of printed planoconvex lens surfaces (**Figure** 4a) were processed to create 3D renders of the curved surface (Figure 4b). The radius of curvature was measured for each radius around the circumference of the lens and plotted as a histogram to calculate the median radius of curvature for each printed lens (Figure 4c). The radii of curvature for three replicate printed lenses of four prescriptions were compared to commercial glass lenses (Figure 4d; Figure S3, Supporting Information). The radius of curvature of 3D printed lenses concurred with their glass counterparts, with a slight increase due to the additive spin coating process. However, this did not hold true for longer focal length lenses, where the increased radius of curvature is more pronounced for longer focal length lenses with larger variations due to the shallower curvature. The mean radius of curvature (± standard deviation) measured; $R\,(f_{+\ 12.5\ \mathrm{mm}})$ = 10.76 ± 1.04 mm, $R\,(f_{+\ 19.9\ \mathrm{mm}})$ = 11.31 ± 0.66 mm, $R\,(f_{+\ 35.0\ \mathrm{mm}})$ = 18.83 ± 0.40 mm, $R\,(f_{+\ 49.8\ \mathrm{mm}})$ = 31.44 ± 4.01 mm. These values compare to the theoretical radii of curvature for their glass counterparts; $R\,(f_{+\ 12.5\ \mathrm{mm}})$ = 9.80 mm, $R\,(f_{+\ 19.9\ \mathrm{mm}})$ = 10.30 mm, $R\,(f_{+\ 35.0\ \mathrm{mm}})$ = 18.10 mm, $R\,(f_{+\ 49.8\ \mathrm{mm}})$ = 25.80 mm.

The IRM images of 3D printed lenses routinely featured a larger-than-expected zeroth order minimum. This suggested that the apex of the convex lenses was flat, but this was not observed in white light interferometry or stylus profilometry experiments (Figure S2, Supporting Information). Moreover, the curvature of the zeroth order area measured using these methods agreed with the theoretical curvature and the median radius of curvature measured by IRM. To conclude that the zeroth order area was curved, a modified z-scanning Tolansky interferometry method was employed (**Figure** 5a). Uncoupling of the lens specimen from the objective setup permitted the translation of the interference orders over the lens surface in unison with the axial movement of the modified objective housing (Figure 5b). A maximum intensity projection from a Tolansky interferometry z-series revealed the nanoscale surface profile and the continuous curved surface of the printed lens (Figure 5c), confirming the observations using white light and stylus profilometry.

3.2. Optical Characterisation of 3D Printed Lenses

3.2.1. Comparing the Transmissivity of 3D Printed Resin to Commercial Glass Lenses

The transmissivity of the 3D print resin substrate was measured to verify the optical properties of the clear resin. The mean

© 2024 The Authors. Advanced Materials Technologies published by Wiley-VCH GmbH

2365709x, 0, Downloaded from https://onlinelibrary.wiley.com/doi/10.1002/admt.202400043 by Welsh Assembly Government, Wiley Online Library on [08/05/2024]. See the Terms and Conditions (https://onlinelibrary.wiley.com/terms-and-conditions) on Wiley Online Library for rules of use; OA articles are governed by the applicable Creative Commons License

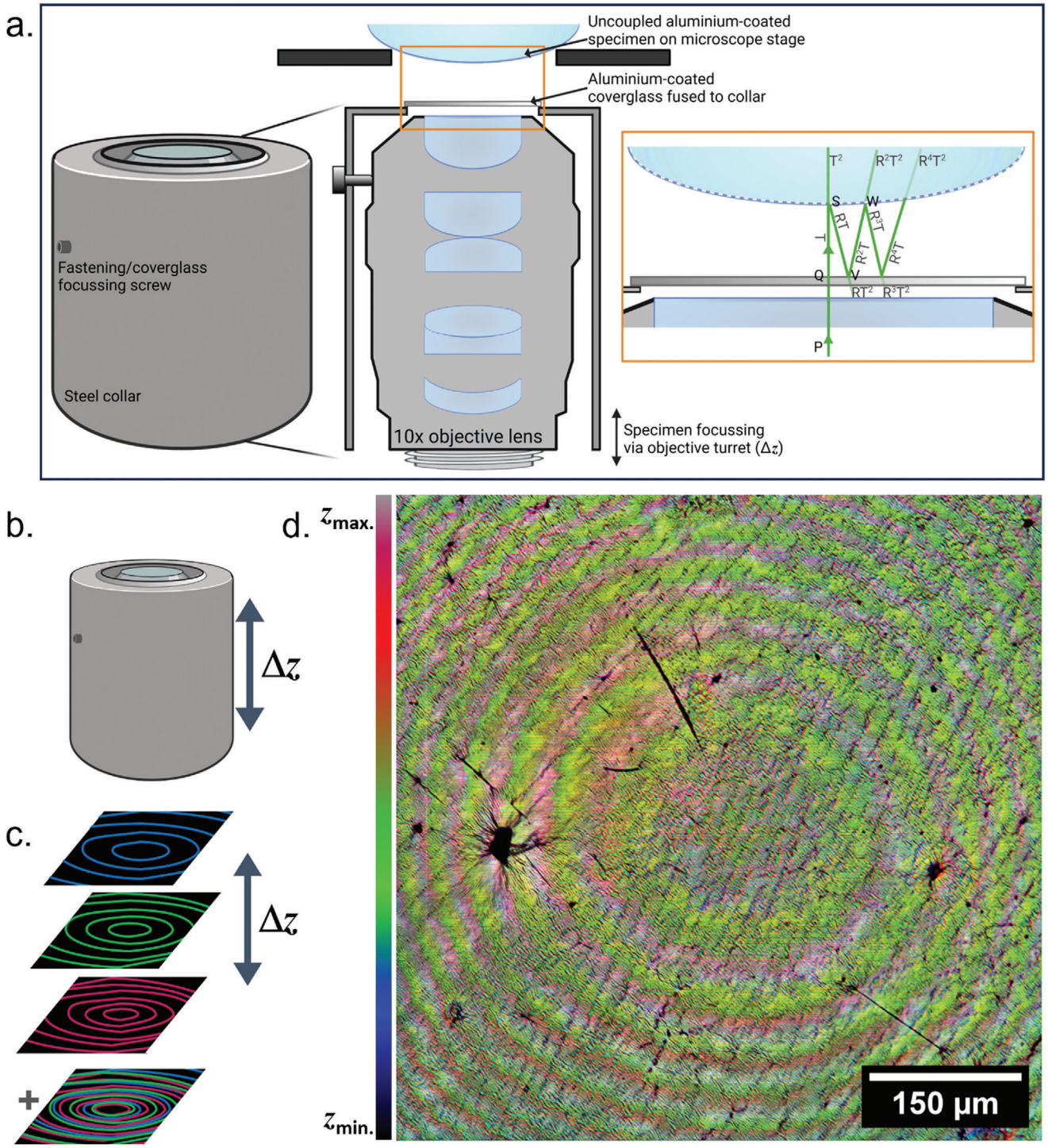

Figure 5. Tolansky Interferometry Confirms the Apical Surface Curvature of 3D Printed Lenses. a) A schematic (not to scale) describing the principles of Tolansky interferometry and the design of a custom objective lens to permit 3D measurements of surface curvature of an aluminum-coated specimen. b) Axial translation of the objective mount results in c) translation of the interference orders, which can be colour-coded by depth and merged into a *z*-projection of a Tolansky interferometry acquisition. d) The concentric interference maxima from each axial position are false coloured according to their depth and super-imposed, revealing the curved surface and nanoscale topology of the apical lens surface with higher resolution than interference optical microscopy can provide.

© 2024 The Authors. Advanced Materials Technologies published by Wiley-VCH GmbH

2365709x, 0, Downloaded from https://onlinelibrary.wiley.com/doi/10.1002/admt.202400043 by Welsh Assembly Government, Wiley Online Library on [08/05/2024]. See the Terms and Conditions (https://onlinelibrary.wiley.com/terms-and-conditions) on Wiley Online Library for rules of use; OA articles are governed by the applicable Creative Commons License

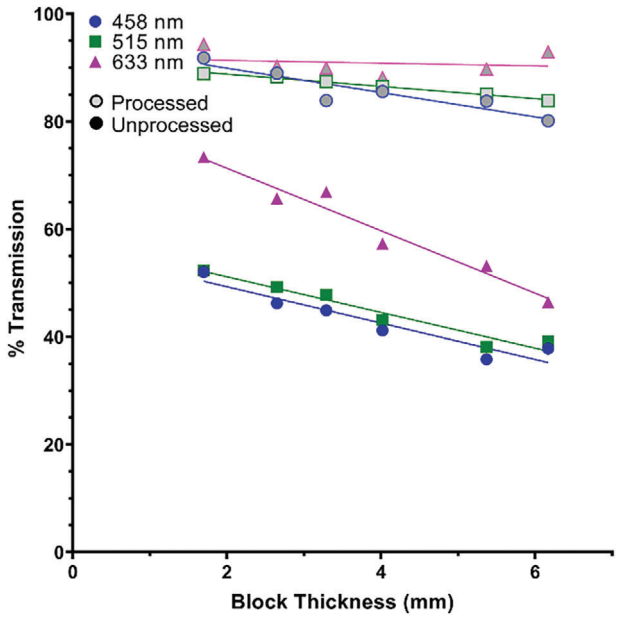

Figure 6. Optical Throughput of Naïve and Post-processed Resin Blocks. Naïve (i.e., unprocessed) blocks (solid markers) exhibited lower optical throughput than processed blocks (hollow markers). Optical throughput was typically higher with longer wavelengths of transmitted light, with processed blocks achieving up to 94.33% transmission at a wavelength of 633 nm.

intensity of the transmitted light was normalized compared to a control of the same intensity of light passing through a Type 1.5 cover glass (**Figure 6**). Block transmissivity was increased by ≈2.25 × up to greater than 90% across all tested wavelengths following spin-coating, comparable to uncoated N-BK7 glass often used to manufacture glass bulk optics.[38]

3.2.2. Measuring the Optical Performance of 3D Printed Lenses

The optical performance of four 3D printed planoconvex lens prescriptions was measured in triplicate using the setup shown in **Figure 7a**. The focal length approximately matched the theoretical values for all lenses, except for $f = 49.8$ mm (Figure 7). The measured focal lengths for each lens prescription were $f_{12.5\ mm} = 13.5$ mm, $f_{19.9\ mm} = 19.0$ mm, $f_{35.0\ mm} = 35.0$ mm. These data presented an error of $f_{12.5\ mm} = 8.0\%$, $f_{19.9\ mm} = -4.5\%$, and $f_{35.0\ mm} = 0.0\%$ compared to the focal lengths of their glass counterparts. The longer theoretical focal length lenses (i.e., $f_{49.8\ mm}$) did not focus the light as expected. The beam profile was elongated along the optical axis at the beam waist and was significantly displaced from the theoretical focal length, indicating the presence of spherical aberration. Each of the printed lenses was compared to the focusing performance of their commercial glass counterparts using the same profiling setup. The glass commercial lenses performed as expected, resulting in the correct focal length for each prescription. 3D Gaussian fits for the beam waist of each 3D printed lens prescription compared to their glass counterparts are presented in Figure S4 (Supporting Information). The beam diameter at the focal point (z_0) was consistently smaller in commercial glass lenses; however, despite the increased beam waist size of 3D printed lenses, there was good agreement with the focal performance expected from theory (shown by the Gaussian profiles).

The beam waist (w_0) and Rayleigh Range were measured for each 3D printed lens and were compared to the commercial glass counterpart, except for the $f_{49.8\ mm}$ lenses due to the severity of the optical aberrations (**Table 1**; Figure S5, Supporting Information). The mean w_0 and the Rayleigh Range values for the lens prescriptions are noted in Table 1. Although the focal length of these 3D printed lenses conformed with their commercial glass counterparts, the mean w_0 value was routinely larger with 3D printed lenses. Moreover, the Rayleigh range was also increased proportionally to the enlarged w_0. However, 3D printed lenses were ultimately able to focus a beam to a discrete point which demonstrated promise for implementation in optical systems.

3.2.3. Using 3D Printed Optics for Brightfield Transmission Imaging

The imaging performance of 3D printed optics was tested using the setup presented in Figure S6 (Supporting Information), where a 3D printed lens ($f = +49.8$ mm) was used as the condenser in a brightfield transmission microscope. The setup resulted in a field of view measuring ≈2.3 mm wide with high contrast across the full field (**Figure 8a**). Moreover, brightfield transmission imaging was demonstrated using a cross-section of a linden tree stem, resolving the intricate differentiated tissue layers and structures on the order of 6 µm (Figure 8b). This sub-cellular resolution demonstrates the potential of 3D printed optics in biological imaging systems.

4. Discussion

We have demonstrated robust, repeatable, and accessible methods to manufacture planoconvex lenses using 3D printing with consumer-grade instrumentation and printing materials. Moreover, we have characterized and compared the quality of 3D printed lenses against commercially available glass counterparts of the same prescription. A spin-coating method was employed to obviate the stepped print structure and to render the printed lenses smooth and transparent, resulting in a thin surface coating on the order of 35 µm thick. White light and stylus profilometry were used to assess the surface quality of printed lenses, while confocal IRM was used to reconstruct the surface topology of 3D printed lenses with high axial resolution and quantify the radius of curvature, which matched that of glass lens counterparts. It is important to note that, while IRM in confocal scanning mode provides increased contrast due to coherent illumination and the rejection of out-of-focus light by a pinhole aperture, widefield IRM also presents feasible and accessible method to achieve similar, albeit lower-contrast, IRM data. Tolansky multiple beam interferometry corroborated the profilometry data by revealing the curved topology of the apex of the convex lenses. The printing and processing steps facilitated comparable optical throughput to glass lenses, with greater than 90% transmission across the visible spectrum. The optical performance of 3D printed lenses was determined by measuring their ability to focus a beam of light. Shorter focal length printed lenses were observed to have the same focal length as their glass counterparts,

© 2024 The Authors. Advanced Materials Technologies published by Wiley-VCH GmbH

2365709x, 0, Downloaded from https://onlinelibrary.wiley.com/doi/10.1002/admt.202400043 by Welsh Assembly Government, Wiley Online Library on [08/05/2024]. See the Terms and Conditions (https://onlinelibrary.wiley.com/terms-and-conditions) on Wiley Online Library for rules of use; OA articles are governed by the applicable Creative Commons License

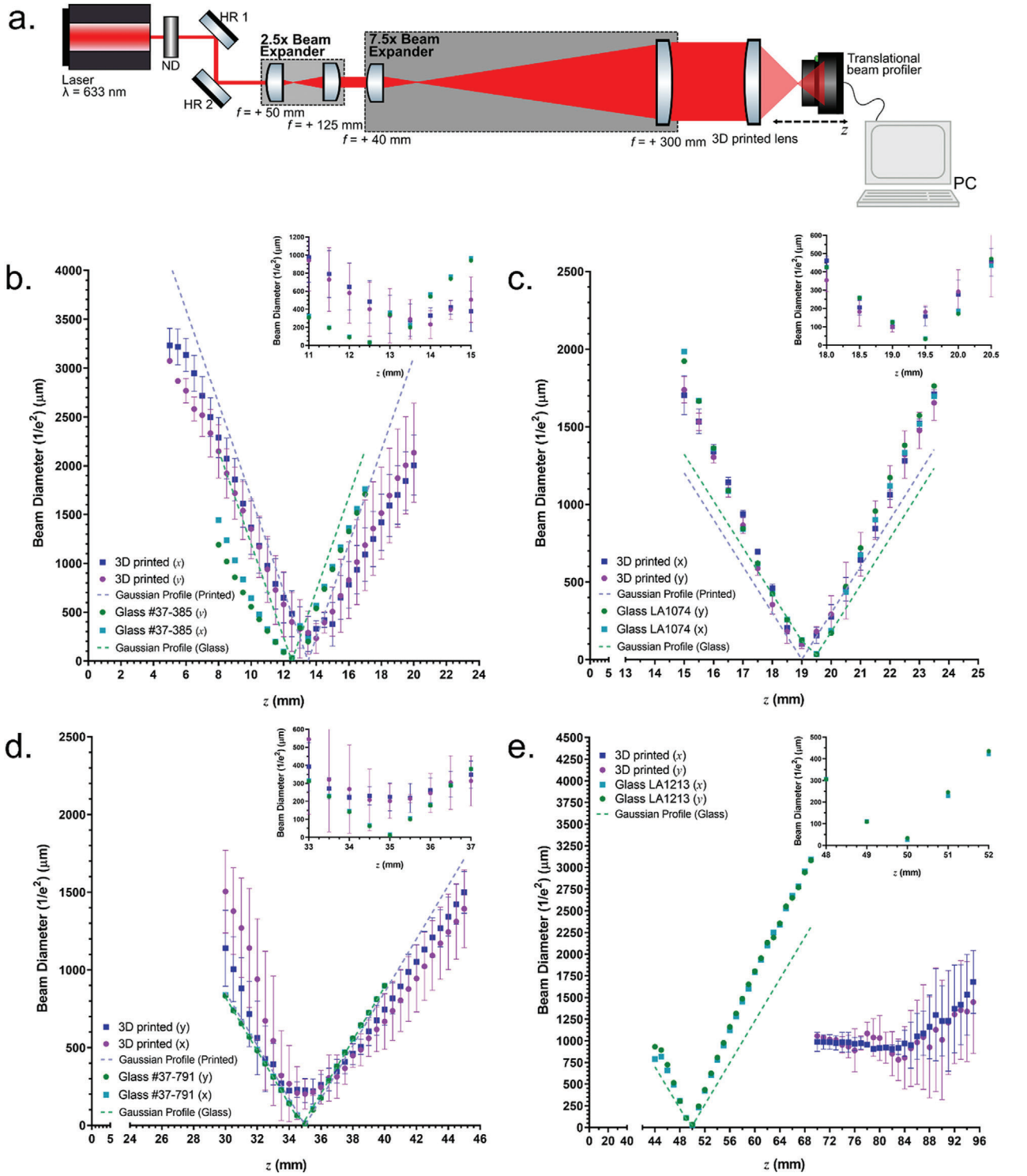

Figure 7. Comparing the Focusing Performance of 3D Printed Lenses. a) An optical setup to measure the beam profile of a 633 nm laser focused by a 3D printed lens. Two concurrent beam expanders provide a total beam expansion of 18.75 ×, creating a 12.5 mm diameter beam that uses the full numerical aperture of the printed lenses. A beam profiler is translated along the optical axis to measure the focal length and metrics of the focused beam. ND = Neutral Density Filter, HR = High Reflector (Mirror), all lenses shown are commercial glass planoconvex lenses, save for the final 3D printed lens under observation. b–e) The beam diameter along the optical axis of several 3D printed lens prescriptions is presented. Both the *x* (blue) and *y* (purple) beam diameters are noted as a function of $1/e^2$. The beam profiles for lenses of theoretical focal length a) + 12.5 mm, b) + 19.9 mm, c) + 35.0 mm, and d) + 49.8 mm are presented. Gaussian fits show the theoretical beam profiles (dashed lines) along with magnified regions of the beam waist are presented as inserts. The focal lengths of (a), (b), and (c) concurred with their theoretical glass counterparts (presented in green for illustration in (b) and (d)) but did not agree for longer focal length lenses in (d).

© 2024 The Authors. Advanced Materials Technologies published by Wiley-VCH GmbH

2365709x, 0, Downloaded from https://onlinelibrary.wiley.com/doi/10.1002/admt.202400043 by Welsh Assembly Government, Wiley Online Library on [08/05/2024]. See the Terms and Conditions (https://onlinelibrary.wiley.com/terms-and-conditions) on Wiley Online Library for rules of use; OA articles are governed by the applicable Creative Commons License

Table 1. Comparison of Beam Parameters in 3D printed and Glass Lenses. The mean beam waist radius (w_0) was measured for three different printed and glass planoconvex lens prescriptions, along with the standard deviation (SD) for three replicate printed lenses. The Rayleigh range (z_R) was calculated for each prescription based on the mean w_0 value.

Lens Prescription	$f_{12.5\ mm}$		$f_{19.9\ mm}$		$f_{35\ mm}$	
	3D Printed	Commercial Glass	3D Printed	Commercial Glass	3D Printed	Commercial Glass
Mean beam waist radius (w_0) (μm) (± SD)	62.40 ± 21.55	16.25	25.26 ± 5.06	17.46	56.67 ± 24.10	6.39
Rayleigh range (z_R) (mm)	19.32	1.31	3.17	1.51	15.93	0.20

with moderately increased beam diameters and Rayleigh ranges. The performance of 3D printed lenses was limited in longer focal length printed lenses (i.e., $f = +49.8$ mm), which exhibited extended focal lengths indicative of spherical aberration. However, our findings present 3D printing as a viable option for the manufacturing of high-quality lenses for optical instrumentation and rapid prototyping as a less costly and more accessible alternative to bulk glass optics. Finally, we demonstrated the use of 3D printed lenses for brightfield transmission imaging. Despite the aberrations observed during beam profilometry experiments using printed $f = +49.8$ mm lenses, the imaging results were promising. Sub-cellular spatial resolution was achieved with high contrast over a 2.3 mm field of view, showing great promise for the use of 3D printed optics in microscopy.

Previous studies developing 3D printed optics have used a variety of additive manufacturing methods, with most of these typically being costly, requiring specialist equipment, or being mainly focused on using consumer-grade printers to produce micro-optics. Fused deposition modeling, where thin glass filaments are melted, extruded and cooled into the shape of a lens, has resulted in 3D printed glass bulk optics.[39] However, the silicon dioxide substrate requires careful mixing with titanium dioxide and a complex series of drying, burnout, and sintering steps performed at over 1000 °C that limit users without access to specialist equipment. Alternative filament-based methods have used CO_2 lasers to print transparent glass lenses from a single-mode optical fiber and fused quartz filaments.[40–42] However, these molten glass methods often result in layering defects that reduce optical performance.

Stereolithography approaches have resulted in various techniques to manufacture resin-based optics. These methods routinely use a two-photon polymerization-based platform to manufacture microlens arrays (MLAs) and optics, although print sizes

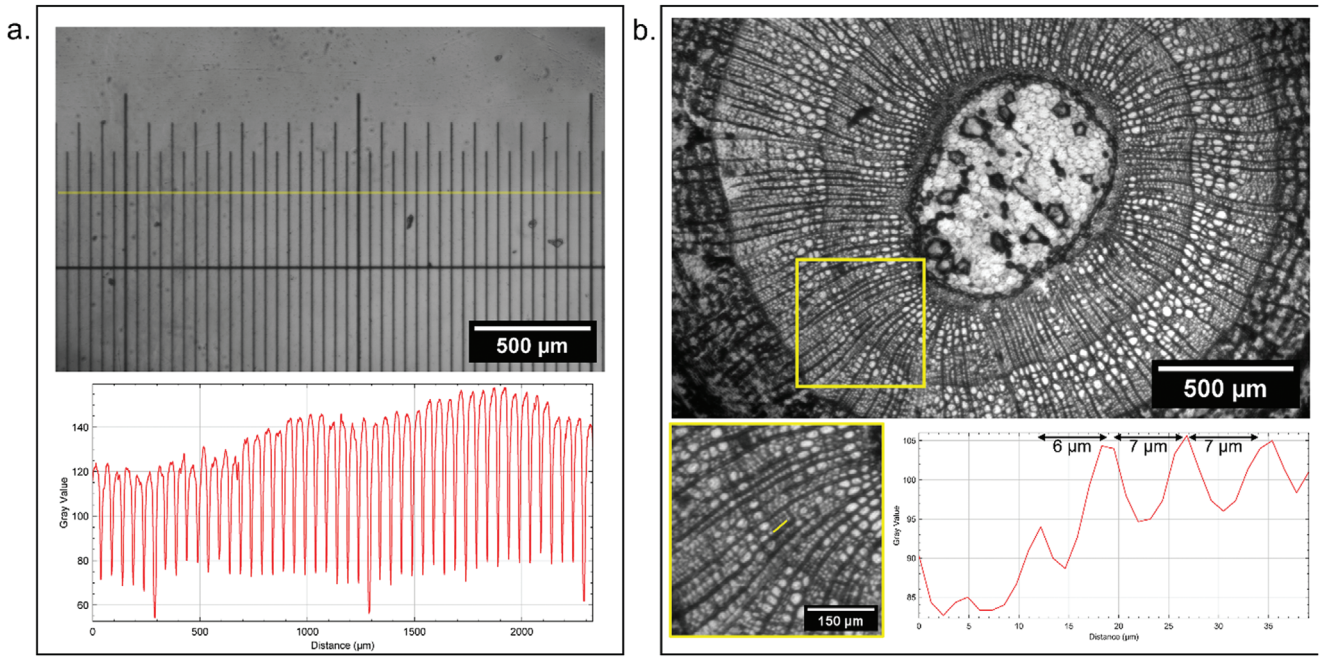

Figure 8. Brightfield Transmission Imaging Using a 3D Printed Condenser Lens. Images demonstrating the application of a 3D printed condenser lens ($f = +49.8$ mm) a) An image of a stage micrometer (R1L3S1P, Thorlabs, USA) measuring a field of view of ≈2.3 mm. A line intensity profile (averaged over 5 pixels thickness) is plotted against distance, showing high contrast across the field of view. b) An image of a linden tree (*Tilia europaea*) stem showing the intricate tissue layers. A magnified region of interest is presented with a yellow box, and this is digitally magnified to show individual plant cells. A line intensity profile (averaged over 5 pixels thickness) is plotted against distance and demonstrates resolution at a level that would be sufficient to record subcellular detail.

© 2024 The Authors. Advanced Materials Technologies published by Wiley-VCH GmbH

2365709x, 0, Downloaded from https://onlinelibrary.wiley.com/doi/10.1002/admt.202400043 by Welsh Assembly Government, Wiley Online Library on [08/05/2024]. See the Terms and Conditions (https://onlinelibrary.wiley.com/terms-and-conditions) on Wiley Online Library for rules of use; OA articles are governed by the applicable Creative Commons License

are typically limited to only a few mm in diameter. Moreover, two-photon-based instrumentation can be prohibitively costly and presents a barrier to entry for accessible 3D printed optics. Printed lenses using, for example, a Nanoscribe printer have recently been produced[43] but they retain microstructures and layering artifacts resulting from the printing process and curvature defects that ultimately impact their optical performance. Moreover, these techniques are often limited by their small print sizes and high materials and instrument costs, somewhat restricting their use to MLAs and other micro-optics. Recent developments in two-photon microprinting have successfully been used to fabricate bespoke micro-optics, such as 30 μm-diameter Fresnel elements for x-ray microscopy, using photopolymerizing resins on a supportive silicon nitride membrane.[44] Foveated compound microlenses have also recently been produced using femtosecond direct laser writing,[18] but all two-photon methods require a costly and complex ultrashort pulsed laser source. Microlens arrays have been printed using UV-induced photopolymerization, with recent improvements seeing expansion of MLAs over large flexible substrates to improve optical performance[45] and the introduction of vibrating projection lenses during printing to smooth the surface of 3D printed micro-optics.[46] Aspheric lenses have been manufactured using UV photopolymerization, however these specialized lenses required assembly with corrective quartz substrates and refractive index matching liquids in order to focus light, but suffered from both chromatic and spherical aberration.[47] Each of these 3D printing methods are based on inaccessible and specialist equipment, which often produces 3D printed lenses that do not compare to the performance of their commercially produced glass counterparts.

We have described an accessible, low-cost, and reproducible method for manufacturing bespoke 3D printed lenses and a suite of characterization methods that demonstrate their comparable performance to glass lenses. We implemented profilometry methods centered on IRM that provide high-resolution topographical reconstructions of the lens geometry, which offer alternative analysis methods for IRM and standing wave microscopy.[26,48] Using 458 nm illumination for IRM and 633 nm light for beam profiling ensured that the material properties of the printed lenses did not change during observation, as the resin absorbance peak is noted as 405 nm. The Tolansky interferometry mapping, together with white light and stylus profilometry data, suggest that the enlarged zeroth order present in IRM images was an inherent interference artifact, perhaps contributed by subtle refractive index differences between the printed layers caused by compounding exposure to light during printing.[49,50] However, despite this apparent interference artifact across all lenses, it did not impact their optical performance. Short focal length lenses with inherently higher curvatures performed in line with their commercial glass counterparts, but longer focal length lenses on the order of $f = 50$ mm were subject to optical aberrations. This suggests that future applications creating 3D printed multi-lens systems would better suit the inclusion of shorter focal length elements. However, there is potential to improve the curvature tolerance of longer focal length lenses (i.e., low curvature) by pre-compensating the coating volume and spin conditions to achieve more uniform shallow surface curvatures. This could then facilitate the implementation of 3D printed lenses in applications that require high precision lenses with a long focal length. Overall, the beam waist radius and Rayleigh range were increased compared to glass lenses, however this did not impact the ability of 3D printed lenses to effectively focus light.

The potential for additive manufacturing for bespoke optics, rapid design prototyping, and field diagnostics is huge. Our data show that high-quality optical elements can be produced at low cost with consumer grade equipment, totaling ≈£300. The only additional outlet would be a spin coater, which can be procured for less than £1000. The total cost of producing a single 3D printed lens was ≈£0.11, as opposed to upward of £50 for commercial high-grade lenses. The demonstrated optical performance of 3D printed lenses shows great promise for optical imaging and prototyping optical instrumentation. Moreover, we have shown separately that 3D printed lenses can be implemented in bioimaging applications, using both absorption and fluorescence imaging modalities.[51] The potential impact of these accessible and open manufacturing methods could also impact low-resource settings for rapid diagnostics of blood smears, for example, where 3D printing has already made significant impacts. The combination of previous 3D printed microscope chassis with 3D printed lenses would be a natural evolution to produce the first fully 3D printed optical microscope.

5. Conclusion

We present an accessible 3D printing method to manufacture high-quality optical lenses and provide characterization methods to quantify their performance. With the prohibitive cost of bespoke bulk glass optics and difficulties in their manufacture, 3D printing offers a viable method to produce a range of lenses with a high degree of reproducibility. The quality of 3D printed lenses was determined by comparing their surface curvature, optical throughput, and ability to focus light compared to their commercial glass counterparts. Glass and 3D printed lenses were observed to behave similarly for a range of short focal length prescriptions, but longer focal lengths introduced a high degree of spherical aberration. The same trend was true for the surface curvature, where highly curved lenses conformed to the radius of curvature of their glass counterparts, while the surface coat thickness was routinely on the order of 35 μm. The transmissivity of 3D printed lenses was comparable to that of bulk N-BK7 glass across the visible spectrum. Moreover, 3D printed lenses were implemented in a brightfield transmission microscopy setup and facilitated high-quality imaging that demonstrated promise for future applications. Each of these observations concluded that 3D printing is a viable approach to reproducibly producing large volumes of high-quality optical elements that provide promise for prototyping, imaging applications, and field diagnostics.

Supporting Information

Supporting Information is available from the Wiley Online Library or from the author.

Acknowledgements

The Authors would like to thank Dr. Ross Scrimgeour (Institute for Cancer Research, UK) for his helpful comments on the IRM analysis code,

© 2024 The Authors. Advanced Materials Technologies published by Wiley-VCH GmbH

2365709x, 0, Downloaded from https://onlinelibrary.wiley.com/doi/10.1002/admt.202400043 by Welsh Assembly Government, Wiley Online Library on [08/05/2024]. See the Terms and Conditions (https://onlinelibrary.wiley.com/terms-and-conditions) on Wiley Online Library for rules of use; OA articles are governed by the applicable Creative Commons License

Mr. Rian MacDonnchadha (University of Glasgow, UK) for his insights on 3D printing instrumentation, and Miss Kay Polland for her assistance with figure preparation. The schematics and workflow presented in Figures 1 and 5 were prepared using BioRender.com (Licence Number: SR25JKZ3PC). L.M.R., S.F., and W.B.A. were funded by the Leverhulme Trust. J.C. and R.B. were funded by the Engineering and Physical Sciences Research Council (grant EP/S032606/1, studentship EP/T517938/1) and the UK Royal Academy of Engineering (Engineering for Development Fellowship scheme RF1516/15/8). B.W. was funded by a Royal Microscopical Society Summer Studentship. L.C. and L.D.W. were funded by an EPSRC iCASE studentship (EP/Y528833/1). G.M. was funded by The Medical Research Council, MR/K015583/1, and the Biotechnology and Biological Sciences Research Council, BB/P02565X/1 and BB/T011602/1.

Conflict of Interest

The authors declare no conflict of interest.

Author Contributions

L.M.R. and J.C. contributed equally to the work. R.B. and G.M. contributed equally to project management and funding. L.M.R. performed conceptualization, data curation, analysis, investigation, methodology, supervision, validation, visualization, and prepared and reviewed the final manuscript. J.C. performed conceptualization, analysis, investigation, methodology, validation, visualization, and prepared and reviewed the final manuscript. B.W. performed analysis, investigation, methodology, validation, software, visualization, and reviewed the final manuscript. Y.S.K. performed analysis, investigation, methodology, validation, visualization, and reviewed the final manuscript. L.C. performed investigation, methodology, and reviewed the final manuscript. L.D.W. performed investigation, methodology, and reviewed the final manuscript. S.F. performed methodology, validation, and reviewed the final manuscript. W.B.A. performed conceptualization, methodology, and reviewed the final manuscript. R.B. performed conceptualization, funding acquisition, project administration, supervision, and reviewed the final manuscript. G.M. performed conceptualization, funding acquisition, project administration, supervision, and reviewed the final manuscript. L.M.R. and J.C. contributed equally to this work as co-1st authors. R.B. and G.M. contributed equally to this work as co-senior authors.

Data Availability Statement

The data that support the findings of this study are openly available in [University of Strathclyde KnowledgeBase] at [doi.org/10.15129/bc849aae-198c-45f3-9e7f-2613532726af], reference number [0].

Keywords

additive manufacturing, optics, open microscopy

Received: January 11, 2024
Revised: March 20, 2024
Published online:

[1] T. Baden, A. M. Chagas, G. Gage, T. Marzullo, L. L. Prieto-Godino, T. Euler, *PLoS Biol.* **2015**, *13*, e1002086.
[2] A. Maia Chagas, L. L. Prieto-Godino, A. B. Arrenberg, T. Baden, *PLoS Biol.* **2017**, *15*, 2002702.
[3] B. Diederich, R. Lachmann, S. Carlstedt, B. Marsikova, H. Wang, X. Uwurukundo, A. S. Mosig, R. Heintzmann, *Nat. Commun.* **2020**, *11*, 5979.
[4] M. Del Rosario, H. S. Heil, A. Mendes, V. Saggiomo, R. Henriques, *Advanced Biology* **2022**, *6*, 2100994.
[5] C. Zhang, N. C. Anzalone, R. P. Faria, J. M. Pearce, *PLoS One* **2013**, *8*, e59840.
[6] J. P. Sharkey, D. C. W. Foo, A. Kabla, J. J. Baumberg, R. W. Bowman, *Rev. Sci. Instrum.* **2016**, *87*, 025104.
[7] J. T. Collins, J. Knapper, J. Stirling, J. Mduda, C. Mkindi, V. Mayagaya, G. A. Mwakajinga, P. T. Nyakyi, V. L. Sanga, D. Carbery, L. White, S. Dale, Z. J. Lim, J. J. Baumberg, P. Cicuta, S. McDermott, B. Vodenicharski, R. Bowman, *Biomed. Opt. Express* **2020**, *11*, 2447.
[8] J. Knapper, J. T. Collins, S. Julian, S. McDermott, W. Wadsworth, R. W. Bowman, *J. Microsc.* **2022**, *285*, 29.
[9] M. L. Rubin, *Surv. Ophthalmol.* **1986**, *30*, 321.
[10] H. Suzuki, S. Hamada, T. Okino, M. Kondo, Y. Yamagata, T. Higuchi, *CIRP Ann.* **2010**, *59*, 347.
[11] E. Brinksmeier, Y. Mutlugünes, F. Klocke, J. C. Aurich, P. Shore, H. Ohmori, *CIRP Ann.* **2010**, *59*, 652.
[12] N. Y. J. Tan, X. Zhang, D. W. K. Neo, R. Huang, K. Liu, A. S. Kumar, *J. Manuf. Process.* **2021**, *71*, 113.
[13] R. Spina, P. Walach, J. Schild, C. Hopmann, *Int. J. Precis. Eng. Manuf.* **2012**, *13*, 2087.
[14] A. Zolfaghari, T. Chen, A. Y. Yi, *Int. J. Extrem. Manuf.* **2019**, *1*, 012005.
[15] M. Falahati, W. Zhou, A. Yi, L. Li, *Appl. Phys. Lett.* **2019**, *114*, 203701.
[16] D. Zhang, X. Liu, J. Qiu, *Front. Optoelectron.* **2021**, *14*, 263.
[17] S. Wu, J. Serbin, M. Gu, *Journal of Photochemistry and Photobiology A: Chemistry* **2006**, *181*, 1.
[18] S. Thiele, K. Arzenbacher, T. Gissibl, H. Giessen, A. M. Herkommer, *Sci. Adv.* **2017**, *3*, e1602655.
[19] Q. Ge, Z. Li, Z. Wang, K. Kowsari, W. Zhang, X. He, J. Zhou, N. X. Fang, *Int. J. Extrem. Manuf.* **2020**, *2*, 022004.
[20] Y. Lu, G. Mapili, G. Suhali, S. Chen, K. Roy, *J. Biomed. Mater. Res.* **2006**, *77A*, 396.
[21] R. Chaudhary, P. Fabbri, E. Leoni, F. Mazzanti, R. Akbari, C. Antonini, *Prog Addit Manuf* **2023**, *8*, 331.
[22] G. Berglund, A. Wisniowiecki, J. Gawedzinski, B. Applegate, T. S. Tkaczyk, *Optica* **2022**, *9*, 623.
[23] G. D. Berglund, T. S. Tkaczyk, *Opt. Continuum* **2022**, *1*, 516.
[24] G. D. Berglund, T. S. Tkaczyk, *Opt. Express* **2019**, *27*, 30405.
[25] J. Schindelin, I. Arganda-Carreras, E. Frise, V. Kaynig, M. Longair, T. Pietzsch, S. Preibisch, C. Rueden, S. Saalfeld, B. Schmid, J.-Y. Tinevez, D. J. White, V. Hartenstein, K. Eliceiri, P. Tomancak, A. Cardona, *Nat. Methods* **2012**, *9*, 676.
[26] L. M. Rooney, L. S. Kölln, R. Scrimgeour, W. B. Amos, P. A. Hoskisson, G. McConnell, *mSphere* **2020**, *5*, 10.
[27] P. W. Tinning, J. K. Schniete, R. Scrimgeour, L. S. Kölln, L. M. Rooney, T. J. Bushell, G. McConnell, *Opt. Lett.* **2023**, *48*, 1092.
[28] S. Tolansky, *An Introduction to Interferometry*, John Wiley & Sons, Inc, New York, NY, **1973**.
[29] H. Verschueren, *J. Cell Sci.* **1985**, *75*, 279.
[30] K. Zuiderveld, In *Graphics Gems*, (Ed: P. S. Heckbert), Academic Press, Cambridge, Massachusetts **1994**, pp. 474–485.
[31] B. Watson, L. M. Rooney, G. McConnell, A computational method to reconstruct the topology of convex lens specimens and calculate their radius of curvature, https://github.com/Liam-M-Rooney/IRM_lenses (accessed: January 2023).
[32] R. Amor, S. Mahajan, W. B. Amos, G. McConnell, *Sci. Rep.* **2014**, *4*, 7359.
[33] S. Tolansky, *Multiple-Beam Interferometry of Surfaces and Films*, Oxford University Press, England, **1948**.
[34] J. E. Lang, G. D. Scott, *J. Opt. Soc. Am.* **1968**, *58*, 81.
[35] W. B. Amos, G. McConnell, T. Wilson, In *Handbook of Comprehensive Biophysics*, Elsevier, Amsterdam, **2011**.
[36] O. Svelto, *Principles of Lasers*, Springer, New York, NY **2010**.

© 2024 The Authors. Advanced Materials Technologies published by Wiley-VCH GmbH

2365709x, 0, Downloaded from https://onlinelibrary.wiley.com/doi/10.1002/admt.202400043 by Welsh Assembly Government, Wiley Online Library on [08/05/2024]. See the Terms and Conditions (https://onlinelibrary.wiley.com/terms-and-conditions) on Wiley Online Library for rules of use; OA articles are governed by the applicable Creative Commons License

[37] L. Walker, L. M. Rooney, G. McConnell, Beam-Profiles-3D-Printed-Lenses, https://github.com/YoItsLewis/Beam-Profiles-3D-Printed-Lenses (accessed: January 2024).
[38] A. Engel, *Opt. Mater. Express* **2022**, *12*, 3776.
[39] R. Dylla-Spears, T. D. Yee, K. Sasan, D. T. Nguyen, N. A. Dudukovic, J. M. Ortega, M. A. Johnson, O. D. Herrera, F. J. Ryerson, L. L. Wong, *Sci. Adv.* **2020**, *6*, eabc7429.
[40] C. Liu, T. Oriekhov, C. Lee, C. M. Harvey, M. Fokine, *3D Print. Addit. Manuf.* **2022**, *11*, 460.
[41] J. M. Hostetler, J. T. Goldstein, D. A. Bristow, R. G. Landers, E. C. Kinzel, In *Laser 3D Manufacturing V*, SPIE, San Francisco, United States, **2018**, p. 6.
[42] J. Luo, J. M. Hostetler, L. Gilbert, J. T. Goldstein, A. M. Urbas, D. A. Bristow, R. G. Landers, E. C. Kinzel, *Opt. Eng.* **2018**, *57*, 041408.
[43] S. Ristok, S. Thiele, A. Toulouse, A. M. Herkommer, H. Giessen, *Opt. Mater. Express* **2020**, *10*, 2370.
[44] U. T. Sanli, H. Ceylan, I. Bykova, M. Weigand, M. Sitti, G. Schütz, K. Keskinbora, *Adv. Mater.* **2018**, *30*, 1802503.
[45] W. Wang, G. Chen, Y. Weng, X. Weng, X. Zhou, C. Wu, T. Guo, Q. Yan, Z. Lin, Y. Zhang, *Sci. Rep.* **2020**, *10*, 11741.
[46] C. Yuan, K. Kowsari, S. Panjwani, Z. Chen, D. Wang, B. Zhang, C. J.-X. Ng, P. V. Alvarado, Q. Ge, *ACS Appl. Mater. Interfaces* **2019**, *11*, 40662.
[47] X. Chen, W. Liu, B. Dong, J. Lee, H. O. T. Ware, H. F. Zhang, C. Sun, *Adv. Mater.* **2018**, *30*, 1705683.
[48] P. W. Tinning, R. Scrimgeour, G. McConnell, *Biomed. Opt. Express* **2018**, *9*, 1745.
[49] M. Schmid, D. Ludescher, H. Giessen, *Opt. Mater. Express* **2019**, *9*, 4564.
[50] M. Reynoso, I. Gauli, P. Measor, *Opt. Mater. Express* **2021**, *11*, 3392.
[51] J. Christopher, L. M. Rooney, M. Donnachie, D. Uttamchandani, G. McConnell, R. Bauer, *Biomed. Opt. Express* **2024**, *15*, 2224.

© 2024 The Authors. Advanced Materials Technologies published by Wiley-VCH GmbH

2365709x, 0, Downloaded from https://onlinelibrary.wiley.com/doi/10.1002/admt.202400043 by Welsh Assembly Government, Wiley Online Library on [08/05/2024]. See the Terms and Conditions (https://onlinelibrary.wiley.com/terms-and-conditions) on Wiley Online Library for rules of use; OA articles are governed by the applicable Creative Commons License